Semiconductor Science and Technology

PAPER

RECEIVED
30 March 2026

REVISED
8 June 2026

ACCEPTED FOR PUBLICATION
12 June 2026

PUBLISHED
25 June 2026

First-principles study on the electron mobilities of aluminum gallium nitrides

Dohee Kim[1], **Arindam Sannyal**[1], **Kisang Byun**[1], **Gyubong Kim**[2], **Sung-Chan Jo**[2,*] and **Joonkyung Jang**[1,*]

[1] Department of Nanofusion Technology, Pusan National University, Busan 46241, Republic of Korea
[2] Samsung Display Co., Ltd., Yongin-si, Gyeonggi-do 17113, Republic of Korea
[*] Authors to whom any correspondence should be addressed.

E-mail: enigma.jo@samsung.com and jkjang@pusan.ac.kr

Keywords: ultra-wide bandgap semiconductor, first-principles calculation, electron mobility, scattering mechanisms

Supplementary material for this article is available online

Abstract

Owing to its ultra-wide bandgap, aluminum gallium nitride (AlGaN) emerges as a promising material for a power semiconductor device. The device performance of AlGaN is mainly governed by its electron mobility. To control the mobility, however, it is desired to understand quantitatively how the mobility relies on its composition and temperature. Using the density functional theory, we investigate the electron mobility of $Al_xGa_{1-x}N$ for the full composition range ($x = 0$–1) by varying temperature from 213 to 673 K. The polar optical phonon scattering is found to primarily limit the mobility, but the piezoelectric scattering becomes important under a low temperature (<240 K) and Al-rich ($x > 0.75$) condition. The present first-principles calculation gives the electron mobilities in accord with those of the prior experimental and theoretical studies. We derive a simple empirical power law which accurately predicts the electron mobility for an arbitrary combination of composition and temperature.

1. Introduction

With the recent advances in the power conversion devices, there are growing demands for semiconductors that can sustain high voltages, high switching speeds, and elevated temperature while maintaining their efficiency and compact form factors [1, 2]. Conventional silicon- (Si-) or gallium arsenide- (GaAs-) semiconductors are limited in their breakdown fields and thermal stabilities because of their narrow bandgaps [1]. Consequently, wide-bandgap materials such as silicon carbide (SiC) (∼2.9 eV) and *gallium nitride* (GaN) (∼3.4 eV) have been extensively utilized in the power switching devices, enabling a dramatic improvement in the size, weight, and power performance [3, 4]. Nevertheless, these materials further need to be improved by developing *ultra-wide-bandgap* (UWBG) materials with bandgaps larger than 3.4 eV.

Among the III-nitride, *aluminum gallium nitride* (AlGaN) underpins the next-generation power and high-frequency electronic devices [4, 5]. In an AlGaN/GaN heterostructure, the discontinuity of polarization at the interface gives rise to a two-dimensional electron gas which enables a high electron mobility transistor (HEMT) [4, 6–8]. The bulk material of AlGaN has also attracted significant interest for its application to a power electronics: the UWBG (⩾3.4 eV), large breakdown field (∼15 MV cm^{-1}), and thermal robustness of AlGaN offer distinct advantages over the conventional semiconductor materials [5, 9]. Such nice properties have motivated the use of AlGaN in a broad range of semiconductor devices, including HEMTs, deep-ultraviolet LEDs, radio-frequency amplifiers, and chemical/biological sensors [10, 11]. In order to transform these material advantages of AlGaN into predictable electrical performance, however, a quantitative understanding of the charge transport in AlGaN is essential [12, 13]. In particular, the electron mobility governs the conductivity of AlGaN and therefore directly contributes to the

on-state resistance, which is a major source of conduction loss in power devices [13, 14]. As the mobility is limited by the electron scattering, it is important to understand how various scattering mechanisms rely on temperature, carrier density, and alloy composition.

The scattering mechanism has been studied previously for GaN. The *ionized impurity* (IMP) scattering is found to be a dominant limitation at a low temperature, while the *polar optical phonon* (POP) scattering dominates at room temperature and higher [15–18]. The electron mobility of $Al_xGa_{1-x}N$ is reported to decrease as the *fraction of* Al_x increases [19–21]. However, it has been challenging to derive a quantitative relationship between the mobility and composition or temperature, because the prior studies employed different growth conditions, and doping levels. Theory and simulation can isolate the effects of composition and temperature by precisely controlling other experimental variables. Unfortunately, the prior theoretical studies on AlGaN have relied on empirical methods, which predict the scattering rates with inputs taken from the interpolation between GaN and AlN [22, 23]. A first-principles study is desired to accurately predict the electron mobility of AlGaN for a given composition and temperature. However, we are unaware of any first-principles studies on the electron mobility of AlGaN [24, 25].

Herein, we report the first-principles study which systematically explores the electron mobility of $Al_xGa_{1-x}N$ for the full composition range ($0 \leqslant x \leqslant 1$) [12, 26–33]. By using the *density functional theory* (DFT), we calculate the structural, electronic, dielectric, piezoelectric (PIE), and elastic properties. These properties are further used for evaluating electron mobility by utilizing the *Boltzmann transport equation* (BTE). We resolve the electron mobility into the contributions from four scattering mechanisms: IMP, POP, *acoustic deformation potential* (ADP), and PIE scattering [12, 34–38]. For a wide range of temperatures relevant to power electronics [3, 13], we derive a simple empirical power law that accurately predicts the electron mobility for a given combination of composition and temperature.

2. Computational methods

We simulate the electronic structure of $Al_xGa_{1-x}N$ by varying x as 0, 0.125, 0.25, 0.375, 0.50, 0.625, 0.75, 0.875, and 1. For a given x, we generate the atomic configurations of $Al_xGa_{1-x}N$ by using the special quasi-random structure (SQS) method implemented in the Alloy Theoretic Automated Toolkit [26]. A $2 \times 2 \times 2$ supercell is constructed from the primitive wurtzite GaN cell, resulting in a 32-atom supercell for each composition. The SQS method generates atomic configurations whose local pair- and short-range correlation functions closely match those of an ideal random alloy, allowing the finite supercell to emulate an $Al_xGa_{1-x}N$ structure at a given composition.

The electronic structure calculations are performed by using the Vienna *Ab initio* Simulation Package [27, 28]. The projector augmented wave method is used to describe the core electrons [29, 30]. We employ the generalized gradient approximation (GGA) in the form of the Perdew–Burke–Ernzerhof functional to model the exchange–correlation functional [31]. A plane wave cutoff of 500 eV is used for all calculations. We relax all the supercell geometries until the maximum force <0.01 eV Å^{-1} and the total energy variation $<10^{-8}$ eV. We carry out the Brillouin zone sampling using a Γ-centered grid with a density of approximately 0.02–0.04 $\times$ 2π Å^{-1}.

As the GGA functionals underestimate the bandgaps, we calculate the bandgap energies by using Heyd–Scuseria–Ernzerhof (HSE06) hybrid functional. We use a fixed (25:75) mixing ratio of Hartree–Fock to GGA and a screening parameter of 0.2 Å^{-1} [39] We compute the PIE stress and dielectric tensors using the *density functional perturbation theory* (DFPT) based on the linear-response theory. We obtain the elastic tensors via the finite difference method by applying small lattice distortions and evaluating the resulting stress response [32, 33, 40]. The elastic tensors are used as input to calculate the ADP and PIE scattering models, and the PIE and dielectric tensors are used as inputs to the mobilities from the PIE, POP, and IMP scattering mechanisms.

The electron mobility and electrical conductivity are calculated by employing the semiclassical BTE. The conductivity tensor at a temperature T, $\sigma_{\alpha\beta}(T)$, is computed from the spectral conductivity $\Sigma_{\alpha\beta}(\varepsilon)$ as

$$\sigma_{\alpha\beta}(T) = e^2 \int \mathrm{d}\varepsilon \Sigma_{\alpha\beta}(\varepsilon) \left(-\frac{\partial f}{\partial \varepsilon}\right) \tag{1}$$

where f is the Fermi–Dirac distribution, α and β denote the Cartesian coordinates. The spectral conductivity tensor is given by

$$\Sigma_{\alpha\beta}(\varepsilon) = \sum_{n,\mathbf{k}} \tau_{n\mathbf{k}} v_{n\mathbf{k},\alpha} v_{n\mathbf{k},\beta} \delta(\varepsilon - \varepsilon_{n\mathbf{k}}), \tag{2}$$

where ε_{nk} and v_{nk} are the energy and group velocity, respectively. In practice, the summation over k represents a Brillouin-zone sampling of the corresponding k-space integral, with the usual volume/normalization factors absorbed into the adopted definitions of $\Sigma_{\alpha\beta}(\varepsilon)$.

The electron mobility at temperature T, $\mu(T)$, given by

$$\mu(T) = \frac{\sigma_{iso}(T)}{ne}, \tag{3}$$

where n is the electron concentration, and e is the elementary charge, and $\sigma_{iso}(T)$ is given by the isotropic average of $\sigma(T)$ the tensor, $\sigma_{iso}(T) = \frac{1}{3}Tr[\sigma(T)]$. The present mobilities are reported for a fixed n-type electron concentration, $n = 5.5 \times 10^{16}\,\mathrm{cm}^{-3}$, chosen to represent a moderately doped in III-nitride mobility and relevant to lightly doped regions used in nitride power devices [15, 41]. Temperature is varied from 213 K to 673 K to cover the operational envelope of III-nitride power devices, ranging from sub-ambient conditions encountered in aerospace and cryogenic applications to elevated-temperature operation beyond the thermal limit of conventional Si electronics (∼423 K) [3, 42]. μs are evaluated on a 20 K grid over 213−673 K, the μ at 300 K is additionally computed explicitly for comparison with room temperature experimental data.

The mode- and state-dependent *relaxation time* τ_{nk} is given by the Fermi's golden rule. For the elastic processes, the transition rate from an initial state $n\mathbf{k}$ to a final state $m\mathbf{k}+\mathbf{q}$ is given by

$$\tilde{\tau}^{-1}_{n\mathbf{k}\to m\mathbf{k}+\mathbf{q}} = \frac{2\pi}{\hbar}|g_{nm}(\mathbf{k},\mathbf{q})|^2\delta\left(\varepsilon_{n\mathbf{k}} - \varepsilon_{m\mathbf{k}+\mathbf{q}}\right), \tag{4}$$

where $g_{nm}(k,q)$ is the electron–phonon (or electron-impurity) coupling matrix element and $\hbar$ is the reduced Planck constant. The inelastic processes include phonon absorption/emission terms with energy conservation $\delta\left(\varepsilon_{n\mathbf{k}} - \varepsilon_{m\mathbf{k}+\mathbf{q}} \pm \hbar\omega_{\mathbf{q}}\right)$, where $\mathbf{q}$ is the phonon wave vector, ω is the phonon angular frequency, and $\hbar\omega$ is the phonon energy. The explicit form of $g_{nm}(\mathbf{k},\mathbf{q})$ for each scattering mechanism is given by Ganose *et al* [34]. The electron–phonon matrix element for the ADP scattering, g^{ADP}_{nm}, is given by [35, 43]

$$g^{\mathrm{ADP}}_{nm}(\mathbf{k},\mathbf{q}) = \sqrt{k_B T}\,\Sigma_{\mathbf{G}\neq-\mathbf{q}}\left[\frac{\widetilde{\mathbf{D}}_{nk}:\hat{\mathbf{S}}_l}{c_l\sqrt{\rho}} + \frac{\widetilde{\mathbf{D}}_{n\mathbf{k}}:\hat{\mathbf{S}}_{t_1}}{c_{t_1}\sqrt{\rho}} + \frac{\widetilde{\mathbf{D}}_{nk}:\hat{\mathbf{S}}_{t_2}}{c_{t_2}\sqrt{\rho}}\right]\left\langle m\mathbf{k}+\mathbf{q}\left|e^{i(\mathbf{q}+\mathbf{G})\cdot\mathbf{r}}\right|n\mathbf{k}\right\rangle, \tag{5}$$

where c_l, c_{t1}, c_{t2} are the sound velocities of the longitudinal and two transverse acoustic modes, obtained from the Christoffel equation using elastic constants [44]; ρ is the mass density. The unit strain tensor for a given acoustic mode is $\hat{\mathbf{S}} = \hat{\mathbf{q}}\otimes\hat{\mathbf{u}}$, where $\hat{\mathbf{q}}$ is the unit vector along phonon propagation and $\hat{\mathbf{u}}$ is the phonon polarization unit vector. Finally, $\widetilde{\mathbf{D}}_{n\mathbf{k}} = \mathbf{D}_{n\mathbf{k}} + \boldsymbol{\nu}_{n\mathbf{k}}\otimes\boldsymbol{\nu}_{n\mathbf{k}}$, where $\mathbf{D}_{n\mathbf{k}}$ is the deformation potential tensor. For the PIE scattering, the electron–phonon matrix element g^{PIE}_{nm} is given by [35, 45, 46]

$$g^{\mathrm{PIE}}_{nm}(\mathbf{k},\mathbf{q}) = \sqrt{k_B T}\,\Sigma_{G\neq-q}\left[\frac{\hat{\mathbf{n}}h:\hat{\mathbf{S}}_l}{c_l\sqrt{\rho}} + \frac{\hat{\mathbf{n}}h:\hat{\mathbf{S}}_{t1}}{c_{t1}\sqrt{\rho}} + \frac{\hat{\mathbf{n}}\mathbf{h}:\hat{\mathbf{S}}_{t2}}{c_{t2}\sqrt{\rho}}\right]\frac{\left\langle m\mathbf{k}+\mathbf{q}\left|e^{i(\mathbf{q}+\mathbf{G})\cdot\mathbf{r}}\right|n\mathbf{k}\right\rangle}{|\mathbf{q}+\mathbf{G}|} \tag{6}$$

where $\hat{\mathbf{n}} = (\mathbf{q}+\mathbf{G})/|\mathbf{q}+\mathbf{G}|$ is the unit vector in the direction of scattering, $\mathbf{h}$ is the PIE stress tensor. The electron–phonon matrix elements for POP (g^{POP}_{nm}) takes the following form [36, 47, 48],

$$g^{\mathrm{POP}}_{nm}(\mathbf{k},\mathbf{q}) = \left[\frac{\hbar\omega_{po}}{2}\right]^{1/2}\Sigma_{G\neq-q}\left(\frac{1}{\hat{\mathbf{n}}\cdot\varepsilon_\infty\cdot\hat{\mathbf{n}}} - \frac{1}{\hat{\mathbf{n}}\cdot\varepsilon_s\cdot\hat{\mathbf{n}}}\right)^{\frac{1}{2}}\frac{\left\langle m\mathbf{k}+\mathbf{q}\left|e^{i(\mathbf{q}+\mathbf{G})\cdot\mathbf{r}}\right|n\mathbf{k}\right\rangle}{|\mathbf{q}+\mathbf{G}|}, \tag{7}$$

where ε_s and ε_∞ are the static and high-frequency dielectric tensors. The IMP matrix element g^{IMP}_{nm} is given by [37]

$$g^{\mathrm{IMP}}_{nm}(\mathbf{k},\mathbf{q}) = \frac{\Sigma_{G\neq-q}n_{ii}^{\frac{1}{2}}}{\hat{\mathbf{n}}\cdot\varepsilon_s\cdot\hat{\mathbf{n}}}\frac{Ze\left\langle m\mathbf{k}+\mathbf{q}\left|e^{i(\mathbf{q}+\mathbf{G})\cdot\mathbf{r}}\right|n\mathbf{k}\right\rangle}{|\mathbf{q}+\mathbf{G}|^2+\beta^2}, \tag{8}$$

where Z is the charge state of the impurity center, e is the electron charge, $n_{ii} = (n_h - n_e)/Z$ is the concentration of ionized impurities, and β is the inverse screening length.

The total electron mobility μ is obtained by enabling all four scattering mechanisms simultaneously to compute the resulting state-dependent lifetime τ_{nk}. Subsequently, $\sigma(T)$ is calculated by using equations (1) and (2) and converting to $\mu(T)$ via equation (3). Note we apply Matthiessen's rule by adding the scattering rates from four scattering mechanisms, $\tau^{-1}_{nk} = \sum_i \tau^{-1}_{i,nk}$ (i = POP, ADP, IMP, PIE).

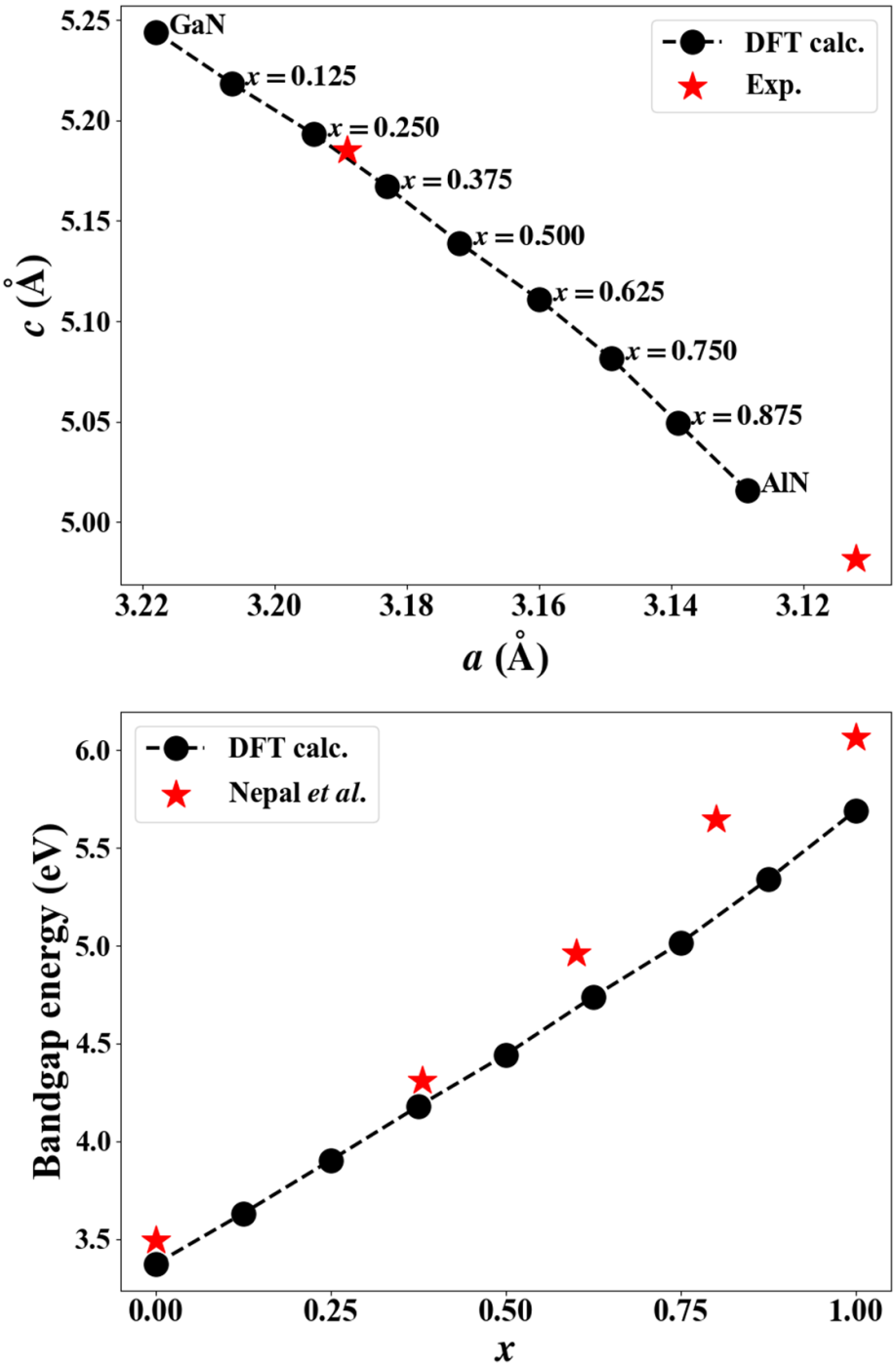

Figure 1. Lattice constants (top) and bandgap energy (bottom) of $Al_xGa_{1-x}N$. The lattice constants a and c (top) and bandgap energy are plotted by varying the fraction of Al, x. Drawn as circles are the present DFT results, and stars as the experimental data. Lines are drawn for visual guide.

The total mobility μ includes the contributions from different scattering mechanisms via equations (1)–(3). It should be noted that this differs from applying Matthiessen's rule for the mobilities of four scattering mechanisms ($\mu^{-1} = \mu_{IMP}^{-1} + \mu_{POP}^{-1} + \mu_{ADP}^{-1} + \mu_{PIE}^{-1}$). We calculate σs and μs by using the AMSET package benchmarked against the GaN experiments with a good accuracy [34].

3. Results and discussion

Figure 1 (top) shows how the wurtzite lattice constants a (=b) and c of $Al_xGa_{1-x}N$ rely on x. The lattice constants for GaN (a = 3.218 Å and c = 5.244 Å) and for AlN (a = 3.129 Å and c = 5.02 Å) accord with the experimental values (a = 3.181 Å and c = 5.193 Å for GaN; a = 3.112 Å and c = 4.982 Å

Table 1. Piezoelectric (e_{ij}) and elastic (C_{ij}) constants of $Al_xGa_{1-x}N$. These data are used for calculation of the contribution of the piezoelectric scattering given by equations (5) and (6).

x in $Al_xGa_{1-x}N$	e_{31} (Cm^{-2})	e_{32} (Cm^{-2})	e_{33} (Cm^{-2})	C_{31} (GPa)	C_{32} (GPa)	C_{33} (GPa)
0 (GaN)	−0.21 (−0.36) [51]	−0.21	0.46 (0.44)[52]	78.15 (70)[53]	78.15 (70)[53]	359.31 (379)[53]
0.06	−0.29	−0.29	0.51	79.49	79.49	361.05
0.13	−0.32	−0.31	0.54	80.40	80.48	361.55
0.19	−0.33	−0.33	0.60	81.92	81.81	365.03
0.25	−0.34	−0.35	0.65	83.44	83.18	367.51
0.31	−0.37	−0.36	0.69	84.13	84.31	367.80
0.50	−0.42	−0.43	0.86	87.12	87.30	367.95
0.63	−0.45	−0.46	1.00	90.02	90.19	368.48
0.75	−0.48	−0.49	1.12	92.95	93.04	367.48
0.87	−0.52	−0.52	1.30	96.00	96.13	363.72
1 (AlN)	−0.56(−0.60) [54]	−0.56	1.44 (1.55) [55]	99.18 (120) [53]	99.18 (120) [53]	360.26 (395) [53]

for AlN), deviating from experiment within 0.05 Å. As x increases, both a and c decrease, consistent with Vegard's law [49]. This contraction arises from the fact that Al is smaller than Ga in atomic size. In figure 1 (bottom), the bandgap energy of $Al_xGa_{1-x}N$ is plotted vs x. The bandgap energy of GaN ($E_g = 3.372$ eV) is in good agreement with the experimental value of 3.495 eV [50]. As x increases from 0 (GaN) to 1 (AlN), the bandgap energy increases. The present bandgap values are consistent with the experimental values reported by Nepal *et al* [50] (4.311, 4.961, 5.649 eV for $x = 0.38$, 0.6, and 0.8, respectively). Overall, the present bandgaps agree with the experimental data with a relative error of less than 10%.

We investigate the dielectric, PIE, and elastic constants from the present DFT calculations. These are used as inputs for the subsequent calculation of the electron mobility by utilizing BTE (see above). The dielectric constant decreases with increasing the Al content: As x increases from 0 (GaN) to 1 (AlN), the high frequency dielectric constant, ε_∞^{xx}, decreases from 5.89 to 4.46, and the static dielectric constant, ε_0^{xx}, decreases from 10.45 to 8.16. This decreasing behavior implies a weaker dielectric screening in the Al-rich alloys, which is expected to strengthen the long-range interactions relevant to both Coulomb impurity scattering and POP coupling. As listed in table 1, the PIE response strengthens with increasing x: e_{31} varies from −0.21 to −0.56 C m^{-2}, and e_{33} from 0.46 to 1.44 C m^{-2}. The elastic constants (table 1) evolve more moderately with changing x: C_{31} and C_{32} increase from 78.15 to 99.18 GPa, and C_{33} varies only weakly across the entire composition range (359.31−368.68 GPa). For the binary endpoints, the present DFT calculation reproduces the overall magnitudes reported in the literature: for GaN, we obtain $e_{31} = -0.21$ C m^{-2}, $e_{33} = 0.46$ C m^{-2}, and $C_{33} = 359.31$ GPa, which are comparable with the reference values, $e_{31} \approx -0.36$ C m^{-2}, $e_{33} \approx 0.44$ C m^{-2}, and $C_{33} \approx 379$ GPa [51–53]. In the case of AlN, $e_{31} = -0.56$ C m^{-2}, $e_{33} = 1.44$ C m^{-2}, and $C_{33} = 360.26$ GPa, which reasonably agree with the reference values of $e_{31} \approx -0.60$ C m^{-2}, $e_{33} \approx 1.55$ C m^{-2}, and $C_{33} \approx 395$ GPa [53–55]. Given these agreements with the literature and the physically reasonable trends with varying the Al fraction, the present dielectric, PIE, and elastic properties seem suitable as inputs for the subsequent calculation of the electron mobility. The PIE tensor e_{31} for GaN is about −0.21 C m^{-2}, while the experimental value is about −0.36 C m^{-2}. The error in the prediction of the PIE scattering rate due to the error in the calculation of the PIE tensor can be estimated as follows. As the PIE matrix and scattering rate are, respectively, linearly and squarely proportional to the PIE tensor, the ratio of the present mobility to the experimental one is estimated as $(-0.36/-0.21)^2 \approx 2.9$. This means the possible error in the calculation of the PIE tensor can lead to an overestimation of the mobility from the PIE scattering by 2.9 times. Note, however, the PIE scattering gives only a minor contribution to the total mobility, except for the high Al fraction at the lowest temperature considered. As shown above, for such a high concentration of Al close to that of AlN, the present total mobility matches the experimental value. Therefore, we do not expect the possible error in the PIE tensor to significantly affect the total mobility overall.

Figure 2 illustrates the electron mobility of $Al_xGa_{1-x}N$ calculated for each scattering (ADP, IMP, PIE, and POP) mechanism. In each panel, the mobility is plotted (color-mapped) as a function of temperature T and x. In all the cases, the n-type carrier concentration is fixed to 5.5×10^{16} cm^{-3}. The mobility limited by the ADP scattering μ_{ADP} (figure 2, upper left) originates from the acoustic phonons that induce elastic distortions and modulate the band edge through the deformation potential [56]. The large elastic constants of GaN and AlN imply high acoustic phonon velocities [57–59] which in turn reduce

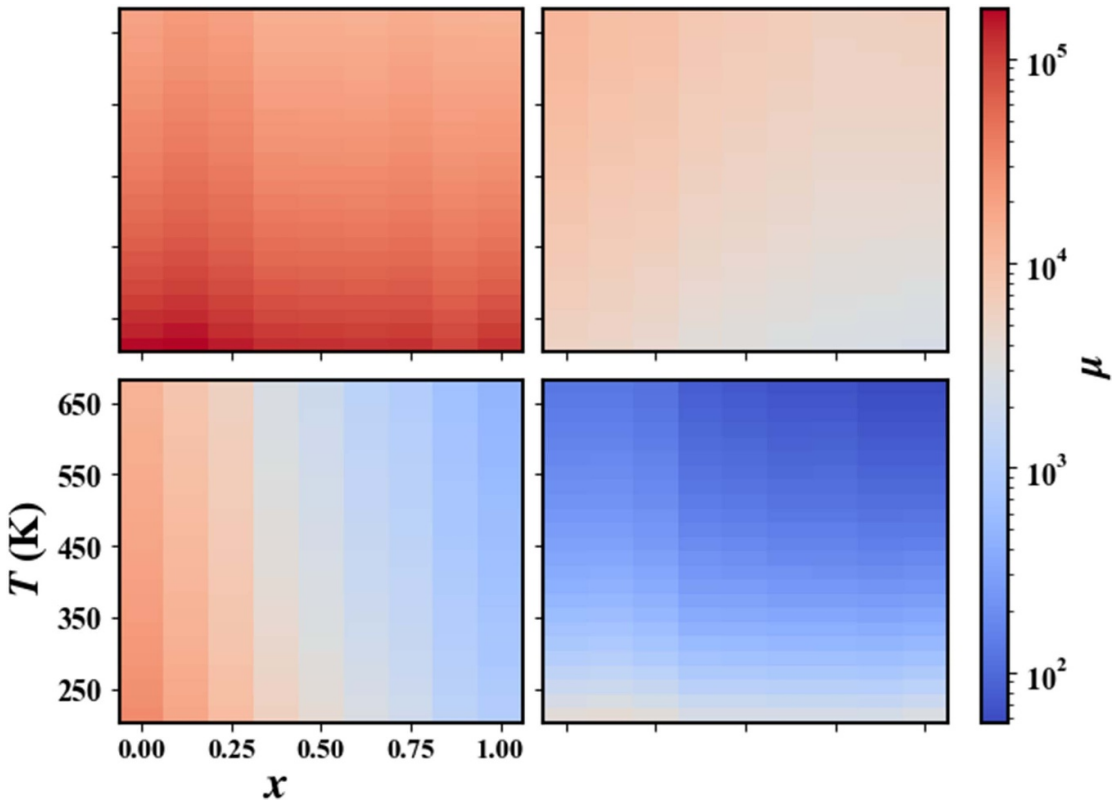

Figure 2. Electron mobility of $Al_xGa_{1-x}N$ color-mapped vs x and temperature T (K). Shown in each panel is the mobility μ ($cm^2\ Vs^{-1}$) arising from a single scattering mechanism: ADP (upper left), IMP (upper right), PIE (lower left), and POP (lower right) scattering. The axis labels and ticks shown in the lower left apply to the rest of the panels.

the ADP matrix element, equation (5), and, therefore, a large value of μ_{ADP}. For example, μ_{ADP} $\sim 1.0 \times 10^5 - 1.75 \times 10^5$ $cm^2\ Vs^{-1}$ at 213 K and $\sim 1.42 \times 10^4 - 2.30 \times 10^4$ $cm^2\ Vs^{-1}$ at 673 K. Hence, the ADP scattering is not a limiting process of electron mobility.

The mobility due to the IMP scattering, μ_{IMP}, (figure 2, top right) is governed by the long-range dielectric screening [56]. Consequently, μ_{IMP} decreases with increasing x, because a weakened dielectric screening of an Al-rich alloy strengthens the screened Coulomb scattering from IMP centers. Quantitatively, at 213 K, μ_{IMP} decreases from 5403 (GaN) to 2463 $cm^2\ Vs^{-1}$ (AlN). At 673 K, μ_{IMP} decreases from 12 504 to 6250 $cm^2\ Vs^{-1}$ as x increases from 0 to 1. Owing to the relatively large values of μ_{IMP}, the IMP scattering is not the main limiting factor of the mobility, but it can be substantial at a low temperature where the POP scattering becomes less severe (see below).

The PIE scattering originates from the fluctuating PIE polarization in a non-centrosymmetric wurtzite crystal and is therefore strongly amplified as the PIE coefficients increase [35]. Resultingly, μ_{PIE} (figure 2, lower left) sensitively relies on x: at 213 K, μ_{PIE} drops from 3.10×10^4 to $1.05 \times 10^3 cm^2\ Vs^{-1}$ with increasing x from 0 to 1. At 673 K, μ_{PIE} decreases from 1.39×10^4 to 485 $cm^2\ Vs^{-1}$ as x increases from 0 to 1. The PIE scattering predominantly limits the electron mobility at a low temperature and Al-rich condition. We find $\mu_{PIE} > \mu_{POP}$ under the condition $x \geqslant 0.75$ and temperature of 213–273 K.

The POP scattering (figure 2, bottom right) arises from the Fröhlich type coupling between electrons and the electric field of *longitudinal optical* (LO) phonons in polar semiconductors [36, 47]. The POP scattering increases rapidly with the LO phonon occupation. This is why the mobility from the POP scattering μ_{POP} mainly depends on temperature but not so much on the composition, as illustrated in figure 2 (bottom right). μ_{POP} ranges from 2357 to 3822 $cm^2\ Vs^{-1}$ at 213 K and from 56.9 to 126.9 $cm^2\ Vs^{-1}$ at 673 K. For the majority of (temperature and composition) conditions studied, μ_{POP} is the lowest among the mobilities originating from four scattering mechanisms. Therefore, the POP scattering primarily limits the electron mobility of AlGaN.

Figure 3 shows the map of the dominant scattering mechanism limiting the electron mobility. For a given combination of x and temperature, the dominant mechanism is defined as the one giving the lowest mobility in figure 2. The POP scattering dominates for the majority of the composition-temperature

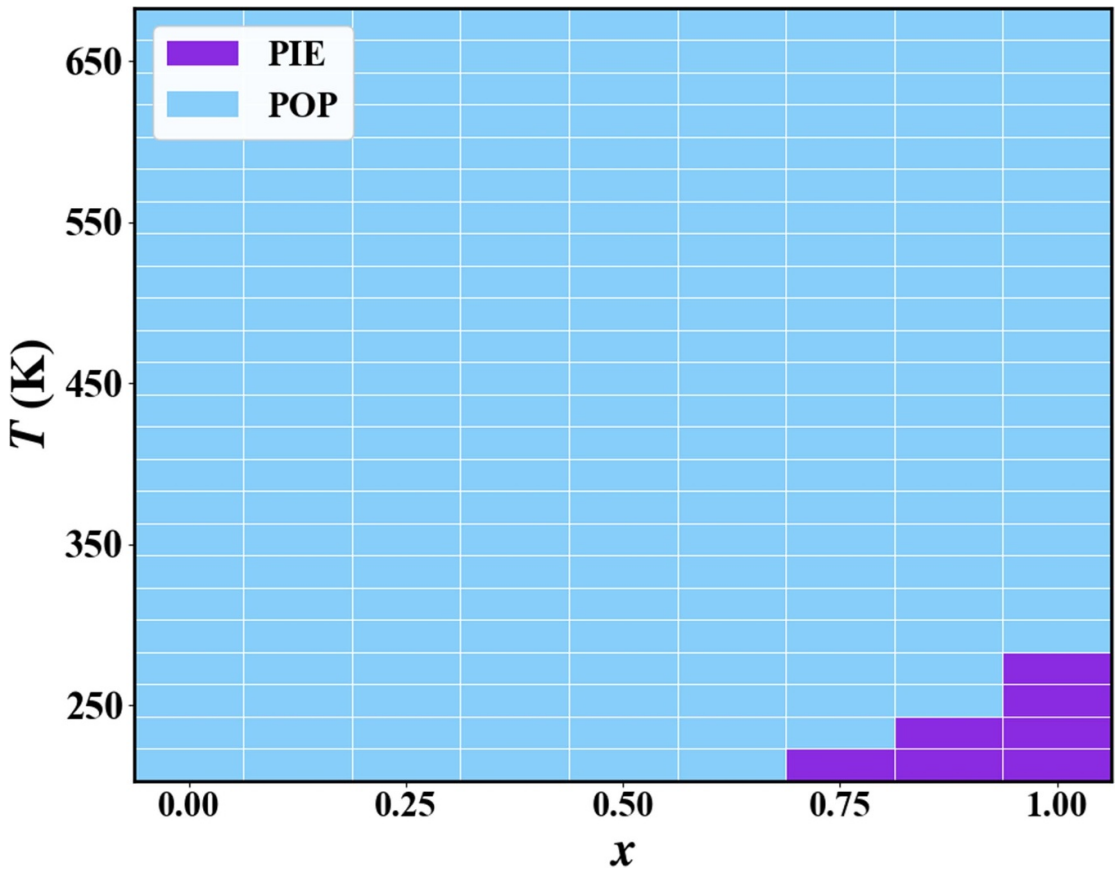

Figure 3. Map of the dominant scattering mechanism of $Al_xGa_{1-x}N$. For a given x and T, the dominant mechanism is defined as the one yielding the smallest among the mobilities from the ADP, IMP, POP, and PIE scattering mechanisms. The POP scattering dominates except for a low-temperature and Al-rich condition where the PIE scattering prevails.

conditions studied. Under an Al-rich and low temperature condition, however, the PIE scattering predominates over the POP scattering: specifically, at $x = 0.75$ at 213 K, $x = 0.875$ at temperature of 213−233 K, and $x = 1$ at $T = 213-273$ K. This PIE dominant region reflects a pronounced strengthening of the PIE coefficients near AlN, where e_{33} increases from 0.46 (GaN) to 1.44 C m^{-2} (AlN), combined with the weakening of the POP scattering at low temperatures where LO phonon occupation is suppressed. Although not shown, the IMP scattering remains secondary to POP and PIE scattering, and the ADP scattering is negligible in all cases.

We now examine the total electron mobility μ by combining the contributions from four scattering (IMP, POP, ADP, and PIE) mechanisms. Shown in figure 4 is μ color-mapped as a function of temperature T and x. Irrespective of x, μ decreases with raising T, reflecting the growth of the POP scattering with elevating temperature. In the case of GaN, μ decreases from 1386.8 to 672.1 and 117.3 cm^2 Vs^{-1} as T rises from 213 to 293 and 673 K. The present mobility of GaN is 672.1 cm^2 Vs^{-1} under the condition of 293 K and $n = 5.5 \times 10^{16}$ cm^{-3}. As summarized in table 2, the present value is comparable to the prior experimental values which decrease from ∼1245 to ∼200 cm^{-2} Vs^{-1} with increasing the donor concentration n from $\sim 6.7 \times 10^{15}$ cm^{-3}) [60] to ∼200 cm^2 Vs^{-1} at $n \sim 10^{17}$ cm^{-3} [18]. As the previous reports were obtained under different carrier concentrations and sample conditions, a rigorous comparison with the present calculation is not feasible, however. We employed the semi-analytic method to model the POP scattering. Recently, however, the full electron–phonon scattering has been considered by using the DFPT and the Wannier function interpolation. In the case of GaN, the present mobility (∼1084 cm^2 Vs^{-1}) agrees well with that from the first-principles study which considered the electron–phonon coupling by utilizing the Wannier functions (905 cm^2 Vs^{-1}) [12].

For AlN, μs are 437.5, 242.2, and 44.6 cm^2 Vs^{-1} at 213, 293, and 673 K, respectively. At $T = 293$ K, for example, μ decreases by 2.8 times (from 672.1–242.2 cm^2 Vs^{-1}) as x increases from 0 to 1. As x increases from 0 to 1, μ decreases by 3.2 times at 213 K and by 2.6 times at 673 K. At a high temperature of 673 K, μ closely matches μ_{POP}: for example, μ and μ_{POP} of GaN are 117.3 are 126.9 cm^2 Vs^{-1}, respectively; μ and μ_{POP} of AlN are 44.6 and 56.9 cm^2 Vs^{-1}, respectively. This signifies that the POP

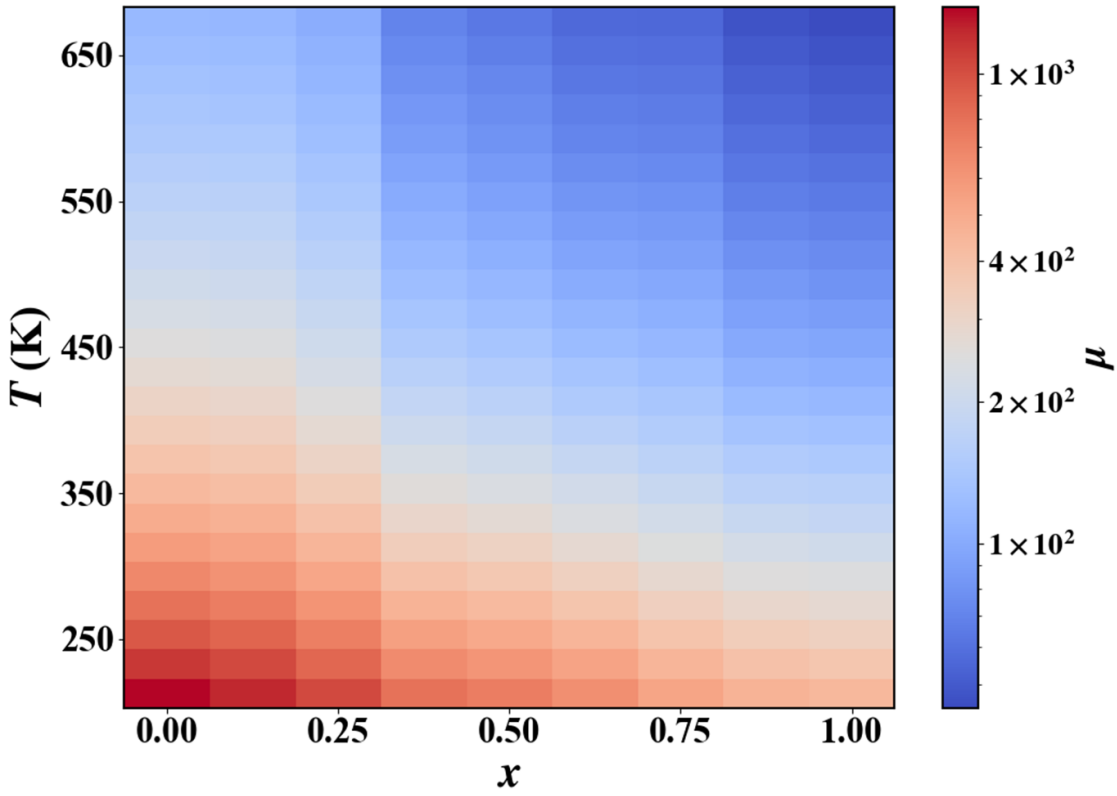

Figure 4. Total mobility of $Al_xGa_{1-x}N$ μ color-mapped as a function of the Al fraction x and temperature T (K). μs are reported in units of $cm^2\ Vs^{-1}$. Note that the color scale is logarithmic.

scattering mainly limits μ at a high temperature. At a low temperature of 213 K however, μ is substantially lower than μ_{POP}: μ and μ_{POP} of GaN are 1386.8 and 3644 $cm^2\ Vs^{-1}$, respectively. This signifies that additional scattering channels (IMP or PIE) make significant contributions when the LO phonon scattering is less severe.

Having obtained the mobility μ of $Al_xGa_{1-x}N$ for the full range of composition by varying temperature, we derive a quantitative scaling law of μ with respect to x and temperature. Such an empirical scaling law can be utilized in predicting the mobility for an arbitrary combination of composition and temperature. Let us first look into the temperature scaling of μ for a fixed composition. Shown in figure 5 is the temperature dependence of μ for given x and T, μ (x,T), divided by the μ at a reference temperature of 293 K with the same composition x, $\frac{\mu(x,T)}{\mu(x,293\,\mathrm{K})}$. The temperature scaling curve is drawn for $x = 0$, 0.25, 0.5, 0.75, and 1. All the scaling curves collapse into one, signifying a universal temperature scaling regardless of x. $\mu(x,T)$ can be well fitted to a power law, $\frac{\mu(x,T)}{\mu(x,293\mathrm{K})} = \left(\frac{T}{293\mathrm{K}}\right)^{-2.103}$. This near-inverse-square temperature scaling seems to be coincidental. Although the total mobility is dominated by the POP scattering, there are quantitatively nonnegligible contributions from the other scattering mechanisms. Table S1 shows the temperature scaling of the mobility originating from each scattering mechanism. Note the scaling exponent of the POP (IMP) scattering decreases (increases) from −2.82 (0.65) to −3.29 (0.82) with increasing the Al fraction x. These opposite signs and trends of the POP and IMP scatterings accidentally give rise to the universal exponent of the temperature scaling. Also, figure S1 illustrates that the contributions of the POP and IMP scatterings remain nearly unchanged across all the Al fractions considered. The POP scattering accounts for 92%–98% of the total scattering rate above the emission threshold, and the IMP scattering remains comparatively small (∼3%–8%) with an opposite temperature trend. As the dominant and secondary scattering contributions remain uniform by varying the Al fraction, the effective temperature scaling exponent also remains constant. The present exponent of temperature scaling is also consistent with those (−1.5 to −2.5) previously reported for III-nitride semiconductors [22, 61, 62].

We next investigate the scaling behavior of μ with respect to the Al fraction x. Shown in figure 6 (top) the scaling behavior of $\mu(x,T)$ divided by μ evaluated for $x = 0$ (GaN) at the same temperature, $\mu(x = 0, T)$. This ratio decreases with increasing x, irrespective of temperature. The curves obtained at different temperatures have similar shapes, but do not show the nearly universal scaling behavior found

Table 2. Comparison of the present calculated electron mobility of GaN ($x = 0$) at $T \approx 300$ K with existing theoretical and experimental values.

Source	Method	T (K)	n (cm^{-3})	μ ($cm^2\ Vs^{-1}$)
This work	DFT + AMSET	293	5.5×10^{16}	672
Look 2001 [60]	Hall measurement	300	6.7×10^{15}	1245
Farahmand 2001 [22]	Monte Carlo	300	$\sim 10^{17}$	~900
Chin 1994 [16]	Variational	300	$\sim 10^{16}$	~1000
Ilegems 1973 [18]	Hall measurement	300	$\sim 10^{17}$	~200
Poncé 2020 [12]	First-principles (EPW)	300	Intrinsic	905

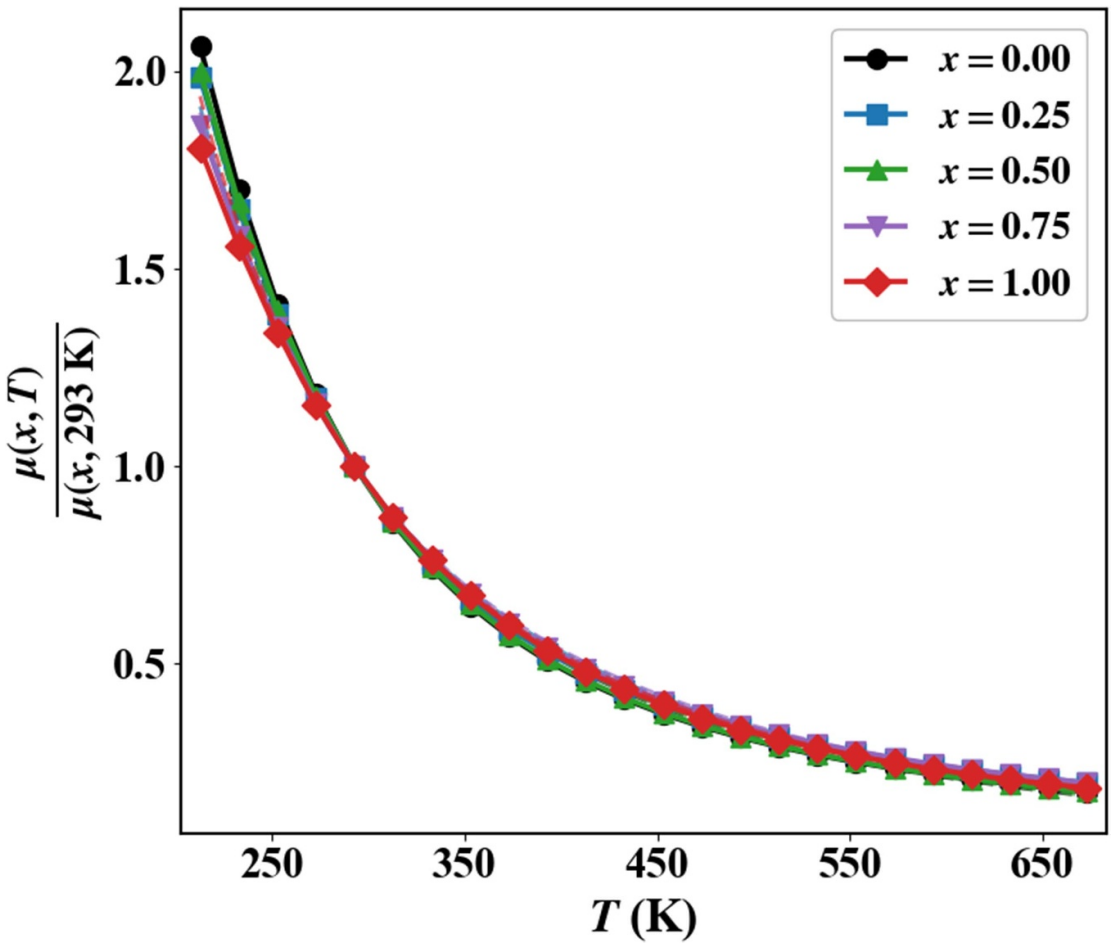

Figure 5. Scaling behavior of the electron mobility of $Al_xGa_{1-x}N$, μ, with respect to temperature T. We plot the temperature dependence of the mobility for given x and temperature T, $\boldsymbol{\mu}\ (x,T)$, divided by the $\boldsymbol{\mu}$ at a reference temperature 293 K. Curves drawn for five different values of x. All the curves can be well fitted to a power law, $\boldsymbol{\mu} \propto \boldsymbol{T^{-2.103}}$ (results not shown here).

with the temperature scaling. At $T = 293$ K, we can fit the composition scaling by the following power law: $\frac{\mu(x,T)}{\mu(x=0,T)} = (1+x)^{-1.507}$ (figure 6, bottom).

Combining the empirical power laws of μ with respect to T and x, the electron mobility of $Al_xGa_{1-x}N$ μ is given by

$$\mu\,(x,T) = \mu_0 \cdot (1+x)^{-1.507} \cdot \left(\frac{T}{293\ K}\right)^{-2.103} \tag{9}$$

where μ_0 (= 672.1 $cm^2\ Vs^{-1}$) is the mobility of GaN at 293 K. As illustrated in figure 7, the scaling law equation (9) agrees well with the present DFT calculation done for nine compositions and 24 temperatures (213–673 K). The present power law gives $R^2 = 0.9887$, a mean absolute error of 5.5%, and a maximum deviation of 18.98%. In particular, the high-temperature subset above 500 K, consisting of 81 data points over 513–673 K and nine compositions, gives a mean absolute deviation of 6.10%, which is comparable to the overall value of 5.50% obtained across 213–673 K. No systematic monotonic increase

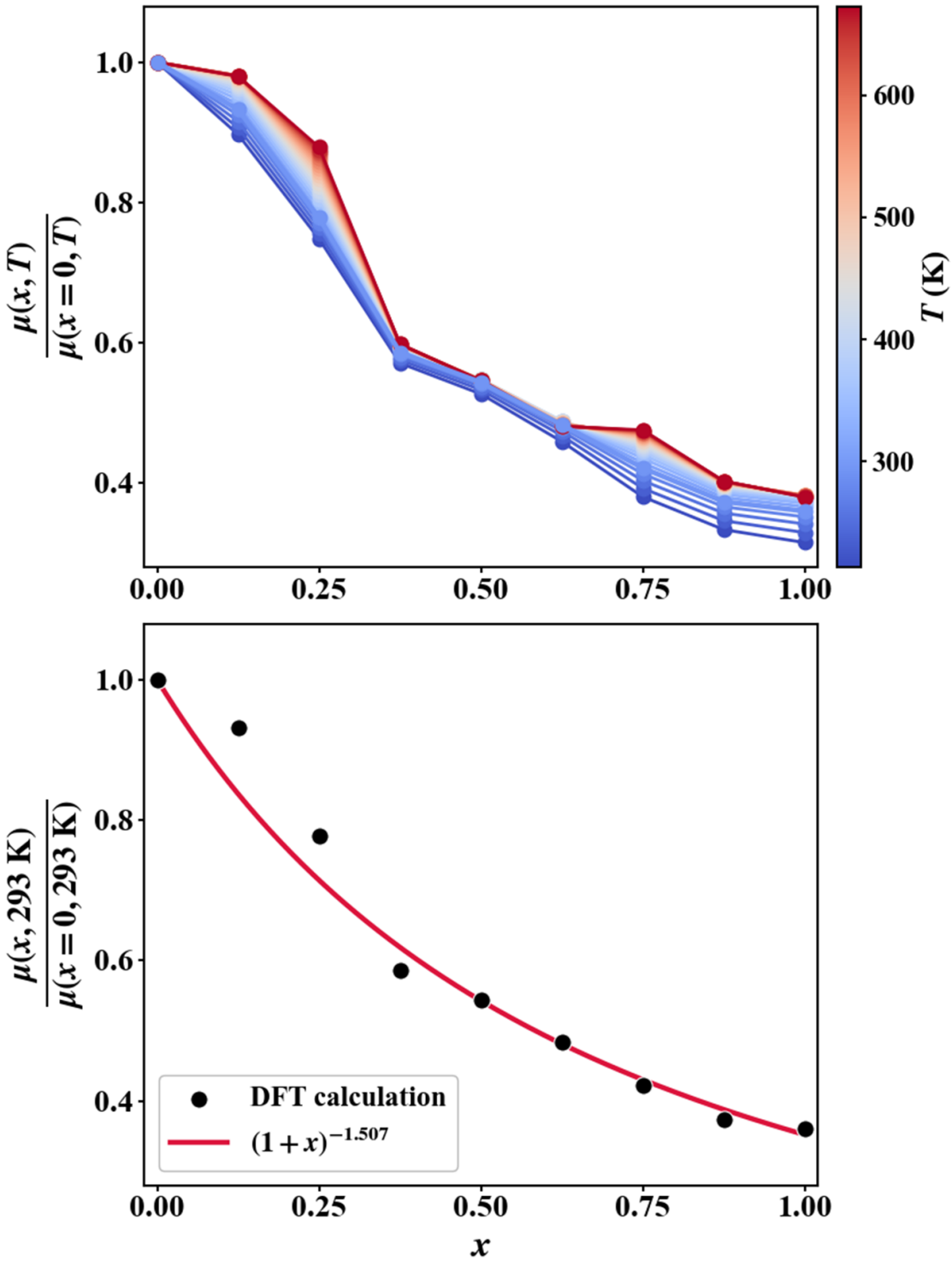

Figure 6. Scaling behavior of the mobility of $Al_xGa_{1-x}N$ with respect to the composition x. (Top) Shown is $\boldsymbol{\mu}(\boldsymbol{x}, \boldsymbol{T})$ divided by $\boldsymbol{\mu}(\boldsymbol{x}=\boldsymbol{0},\ \boldsymbol{T})$ vs x. The composition scaling is drawn by varying T from 213 to 673 K. Lines serve as visual guide. The color scale (blue to red) indicates increasing temperature as shown by the color bar. (Bottom) $\boldsymbol{\mu}(\boldsymbol{x}, \mathbf{T} = \mathbf{293\ K})$ (drawn as circles) fitted to a power law (solid line): $\frac{\mu(x,T)}{\mu(x=0,T)} = (\mathbf{1}+\boldsymbol{x})^{-\mathbf{1.507}}$.

in the deviation is observed with increasing temperature in this range, supporting the applicability of the present scaling law at elevated temperatures considered in this work. The present power law can be utilized to evaluate the electron mobility of $Al_xGa_{1-x}N$ for an arbitrary combination of composition and temperature. The alloy disorder scattering arising from an inhomogeneous distribution of ions cannot be captured by the present DFT study employing a finite-sized supercell. The prior theoretical work on the alloy scattering was largely empirical in that the mobility of AlGaN was interpolated from the known properties of GaN and AlN, such as bandgaps, effective masses, and deformation potentials.

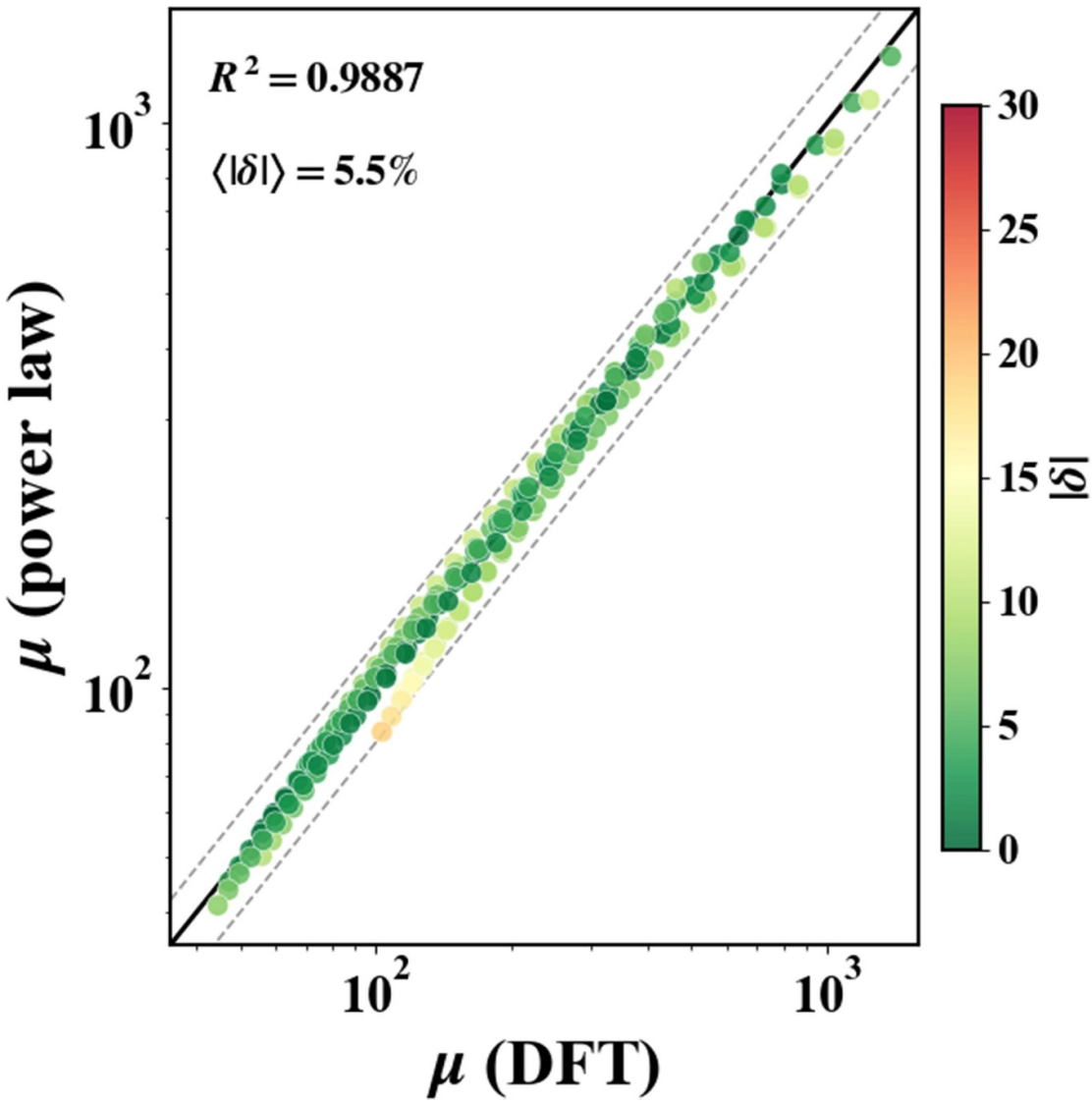

Figure 7. Statistical performance of the empirical power law for the electron mobility, equation (9). The mobilities predicted by the power law, μ (power law)s, are plotted vs those (total of 216) from the present DFT calculations (drawn as circles). Each circle is color-coded by its relative prediction error $|\delta| = |\mu\,(\text{power law}) - \mu\,(\text{DFT})|\,/\,\mu\,(\text{DFT}) \times 100$ (%). The solid diagonal line denotes a perfect agreement, and the dashed lines indicate ±20% deviation bounds. The power law gives $R^2 = 0.9887$ with a mean absolute error of 5.5%.

The total mobility was further obtained by applying the Matthiessen rule by summing up the mobilities from different scattering mechanisms. Including the empirical mobility from the alloy scattering is inconsistent with the present first-principles approach, which calculates the mobility without requiring any empirical data. Note also that the present study applies the Matthiessen rule for the relaxation rate, not for mobility. And the mobility is related to the relaxation rate via the nonlinear relationship given by equation (1). Therefore, the total mobility of the present study cannot be dissected into the contributions from different scattering mechanisms. Admittedly, however, the absence of an alloy disorder scattering presumably limits the quantitative accuracy of the present model, especially at intermediate Al fractions. The previous study reported that alloy scattering is maximal near $x \approx 0.5$–0.6 at 300 K [20]. Inclusion of the alloy scattering mechanism might change the composition dependence of the mobility found in this work. Consideration of the alloy scattering in the first-principles study seems challenging and is left as future work.

Also, the present POP scattering is limited to the single phonon scattering but, in principle, the higher order phonon processes can further decrease the mobility, especially at a high temperature. A previous first-principles study showed that two-phonon scattering can provide an additional scattering channel in a polar semiconductor in GaAs [63]. However, its quantitative contribution in AlGaN remains to be examined in future work.

4. Conclusion

Owing to its UWBG, an AlGaN alloy is considered as a promising material for a power conversion application. By utilizing the first-principles calculations, we investigated the electronic and transport properties of $Al_xGa_{1-x}N$ for the entire range of composition ($x = 0$–1) and for a wide range of temperature (213−673 K). The structural, electronic, dielectric, PIE, and elastic properties were evaluated, and the computed properties for GaN and AlN agree well with experimental and theoretical references. Qualitatively, with increasing the Al fraction of $Al_xGa_{1-x}N$, the lattice constants decrease, the band gap increases, the dielectric screening weakens, and the PIE response strengthens.

The electron mobility of AlGaN was evaluated by employing the semiclassical BTE utilizing the present DFT results as inputs. The mobilities due to four scattering (ADP, IMP, PIE, and POP) mechanisms were calculated and compared with each other. The POP scattering primarily limits the electron mobility for the majority of the temperature-composition conditions studied. This originates from the fact that in the polar nitrides the electron–phonon interaction strongly increases the scattering rate as temperature rises [22, 64]. Under a low temperature and Al-rich condition ($x \geqslant 0.75$ at 213 K, for example), the PIE scattering predominates the mobility. The IMP scattering is enhanced with increasing x because of a reduced dielectric screening, but it remains secondary to the POP or PIE scattering. The ADP scattering was negligible in all cases. The total electron mobility was calculated by combining the relaxation rates from four scattering mechanisms. Qualitatively, the total mobility of $Al_xGa_{1-x}N$ decreases with increasing temperature and with increasing x. We derived a simple power law which accurately predicts the mobility μ for given T and x: $\mu \propto (1+x)^{-1.507}\, T^{-2.103}$. This power law can be easily utilized to evaluate the electron mobility for an arbitrary combination of composition and temperature.

Acknowledgments

This work was supported by Samsung Display Co., Ltd. This work was also supported by Basic Science Research Program through the National Research Foundation of Korea (NRF) funded by the Ministry of Education (RS-2025-25421128).

Data availability statement

All data that support the findings of this study are included within the article (and any supplementary files).

Supplementary data available at https://doi.org/10.1088/1361-6641/ae7ca8/data1.

Author contributions

Dohee Kim 0000-0003-2942-5312
Conceptualization (equal), Formal analysis (equal), Investigation (equal), Methodology (equal), Software (equal), Visualization (equal), Writing – original draft (equal)

Arindam Sannyal 0000-0002-8376-7017
Formal analysis (equal), Investigation (equal), Methodology (equal)

Kisang Byun 0000-0001-6648-2792
Investigation (equal), Writing – review & editing (equal)

Gyubong Kim
Writing – review & editing (equal)

Sung-Chan Jo
Conceptualization (equal), Funding acquisition (equal), Project administration (equal), Supervision (equal), Writing – review & editing (equal)

Joonkyung Jang 0000-0001-9028-0605
Conceptualization (equal), Funding acquisition (equal), Project administration (equal), Resources (equal), Supervision (equal), Writing – review & editing (equal)

References

[1] Chaudhary O S, Denaï M, Refaat S S and Pissanidis G 2023 Technology and applications of wide bandgap semiconductor materials: current state and future trends *Energies* **16** 6689 (In French)
[2] Klein B A *et al* 2023 AlGaN high electron mobility transistor for high-temperature logic *J. Microelectron. Electron. Packag.* **20** 1–8
[3] Amano H *et al* 2018 The 2018 GaN power electronics roadmap *J. Phys. D: Appl. Phys.* **51** 163001
[4] Mishra U K, Parikh P and Yi-feng W 2002 AlGaN/GaN HEMTs-an overview of device operation and applications *Proc. IEEE* **90** 1022–31
[5] Kaplar R J, Allerman A A, Armstrong A M, Crawford M H, Dickerson J R, Fischer A J, Baca A G and Douglas E A 2017 Review—ultra-wide-bandgap AlGaN power electronic devices *ECS J. Solid State Sci. Technol.* **6** Q3061–Q6
[6] Ambacher O *et al* 1999 Two-dimensional electron gases induced by spontaneous and piezoelectric polarization charges in N- and Ga-face AlGaN/GaN heterostructures *J. Appl. Phys.* **85** 3222–33
[7] Ambacher O *et al* 2000 Two dimensional electron gases induced by spontaneous and piezoelectric polarization in undoped and doped AlGaN/GaN heterostructures *J. Appl. Phys.* **87** 334–44
[8] Asif Khan M, Bhattarai A, Kuznia J N and Olson D T 1993 High electron mobility transistor based on a GaN-AlxGa1−xN heterojunction *Appl. Phys. Lett.* **63** 1214–5
[9] Mehta J, Abid I, Elwaradi R, Cordier Y and Medjdoub F 2023 Robust Al0.23Ga0.77N channel HFETs on bulk AlN for high voltage power electronics. e-prime—advances in electrical engineering *Electron. Energy* **5** 100263
[10] Mounika B, Ajayan J, Bhattacharya S and Nirmal D 2022 Recent developments in materials, architectures and processing of AlGaN/GaN HEMTs for future RF and power electronic applications: a critical review *Micro Nanostruct.* **168** 207317
[11] Raj Kumar J S, Du John HV, Iv BKJ, Ajayan J and Nirmal D A 2023 A comprehensive review of AlGaN/GaN high electron mobility transistors: architectures and field plate techniques for high power/ high frequency applications *Microelectron. J.* **140** 105951
[12] Poncé S, Li W, Reichardt S and Giustino F 2020 First-principles calculations of charge carrier mobility and conductivity in bulk semiconductors and two-dimensional materials *Rep. Prog. Phys.* **83** 036501
[13] Lutz J, Schlangenotto H, Scheuermann U and De Doncker R 2018 *Semiconductor Power Devices—Physics, Characteristics, Reliability* (Springer) (https://doi.org/10.1007/978-3-319-70917-8)
[14] Hudgins J L, Simin G S, Santi E and Khan M A 2003 An assessment of wide bandgap semiconductors for power devices *IEEE Trans. Power Electron.* **18** 907–14
[15] Mnatsakanov T T, Levinshtein M E, Pomortseva L I, Yurkov S N, Simin G S and Asif Khan M 2003 Carrier mobility model for GaN *Solid-State Electron.* **47** 111–5
[16] Chin V W L, Tansley T L and Osotchan T 1994 Electron mobilities in gallium, indium, and aluminum nitrides *J. Appl. Phys.* **75** 7365–72
[17] Schwierz F 2005 An electron mobility model for wurtzite GaN *Solid-State Electron.* **49** 889–95
[18] Ilegems M and Montgomery H C 1973 Electrical properties of n-type vapor-grown gallium nitride *J. Phys. Chem. Solids* **34** 885–95
[19] Bellotti E, Bertazzi F and Goano M 2007 Alloy scattering in AlGaN and InGaN: a numerical study *J. Appl. Phys.* **101** 123706
[20] Coltrin M E and Kaplar R J 2017 Transport and breakdown analysis for improved figure-of-merit for AlGaN power devices *J. Appl. Phys.* **121** 055706
[21] Rajan S, DenBaars S P, Mishra U K, Xing H and Jena D 2006 Electron mobility in graded AlGaN alloys *Appl. Phys. Lett.* **88** 042103
[22] Farahmand M, Garetto C, Bellotti E, Brennan K F, Goano M, Ghillino E, Ghione G, Albrecht J D and Ruden P P 2001 Monte Carlo simulation of electron transport in the III-nitride wurtzite phase materials system: binaries and ternaries *IEEE Trans. Electron Devices* **48** 535–42
[23] Hamaguchi C 2021 Electron and hole mobilities of GaN with bulk, quantum well, and HEMT structures *J. Appl. Phys.* **130** 125701
[24] Kyrtsos A, Matsubara M and Bellotti E 2019 First-principles study of the impact of the atomic configuration on the electronic properties of $Al x Ga_1-x N$ alloys *Phys. Rev. B* **99** 035201
[25] Dridi Z, Bouhafs B and Ruterana P 2003 First-principles investigation of lattice constants and bowing parameters in wurtzite AlxGa1−xN, InxGa1−xN and InxAl1−xN alloys *Semicond. Sci. Technol.* **18** 850
[26] van de Walle A, Asta M and Ceder G 2002 The alloy theoretic automated toolkit: a user guide *Calphad* **26** 539–53
[27] Kresse G and Furthmüller J 1996 Efficient iterative schemes for ab initio total-energy calculations using a plane-wave basis set *Phys. Rev. B* **54** 11169–86
[28] Kresse G and Furthmüller J 1996 Efficiency of *ab-initio* total energy calculations for metals and semiconductors using a plane-wave basis set *Comput. Mater. Sci* **6** 15–50
[29] Blöchl P E 1994 Projector augmented-wave method *Phys. Rev. B* **50** 17953–79
[30] Kresse G and Joubert D 1999 From ultrasoft pseudopotentials to the projector augmented-wave method *Phys. Rev. B* **59** 1758–75
[31] Perdew J P, Burke K and Ernzerhof M 1996 Generalized gradient approximation made simple *Phys. Rev. Lett.* **77** 3865–8
[32] King-Smith R D and Vanderbilt D 1993 Theory of polarization of crystalline solids *Phys. Rev. B* **47** 1651–4
[33] Vanderbilt D and King-Smith R D 1993 Electric polarization as a bulk quantity and its relation to surface charge *Phys. Rev. B* **48** 4442–55
[34] Ganose A M, Park J, Faghaninia A, Woods-Robinson R, Persson K A and Jain A 2021 Efficient calculation of carrier scattering rates from first principles *Nat. Commun.* **12** 2222
[35] Zook J D 1964 Piezoelectric scattering in semiconductors *Phys. Rev.* **136** A869–A78
[36] Fröhlich H 1954 Electrons in lattice fields *Adv. Phys.* **3** 325–61
[37] Herring C and Vogt E 1956 Transport and deformation-potential theory for many-valley semiconductors with anisotropic scattering *Phys. Rev.* **101** 944–61
[38] Lundstrom M 2002 Fundamentals of carrier transport 2ndedn *Meas. Sci. Technol.* **13** 230
[39] Krukau A V, Vydrov O A, Izmaylov A F and Scuseria G E 2006 Influence of the exchange screening parameter on the performance of screened hybrid functionals *J. Chem. Phys.* **125** 224106
[40] Resta R 1994 Macroscopic polarization in crystalline dielectrics: the geometric phase approach *Rev. Mod. Phys.* **66** 899–915
[41] Ridley B K, Foutz B E and Eastman L F 2000 Mobility of electrons in bulk GaN and $ Al x Ga 1-x N GaN$ heterostructures *Phys. Rev. B* **61** 16862–9
[42] Nela L, Perera N, Erine C and Matioli E 2021 Performance of GaN power devices for cryogenic applications down to 4.2 K *IEEE Trans. Power Electron.* **36** 7412–6
[43] Born M 1926 Quantenmechanik der Stoßvorgänge *Z. Phys.* **38** 803–27 (In German)
[44] Auld B A 1973 *Acoustic Fields and Waves in Solids* vol 1 (Wiley)

[45] Meijer H J G and Polder D 1953 Note on polar scattering of conduction electrons in regular crystals *Physica* **19** 255–64
[46] Harrison W A 1956 Mobility in zinc blende and indium antimonide *Phys. Rev.* **101** 903
[47] Verdi C and Giustino F 2015 Fr\"ohlich electron-phonon vertex from first principles *Phys. Rev. Lett.* **115** 176401
[48] Sjakste J, Vast N, Calandra M and Mauri F 2015 Wannier interpolation of the electron-phonon matrix elements in polar semiconductors: polar-optical coupling in GaAs *Phys. Rev. B* **92** 054307
[49] Vegard L 1921 Die Konstitution der Mischkristalle und die Raumfüllung der Atome *Z. Phys.* **5** 17–26 (In German)
[50] Nepal N, Li J, Nakarmi M L, Lin J Y and Jiang H X 2005 Temperature and compositional dependence of the energy band gap of AlGaN alloys *Appl. Phys. Lett.* **87** 242104
[51] O'clock G D Jr and Duffy M T 1973 Acoustic surface wave properties of epitaxially grown aluminum nitride and gallium nitride on sapphire *Appl. Phys. Lett.* **23** 55–56
[52] Bykhovski A D, Gelmont B L and Shur M S 1997 Elastic strain relaxation and piezoeffect in GaN-AlN, GaN-AlGaN and GaN-InGaN superlattices *J. Appl. Phys.* **81** 6332–8
[53] Ambacher O 1998 Growth and applications of group III-nitrides *J. Phys. D: Appl. Phys.* **31** 2653–710
[54] Bernardini F, Fiorentini V and Vanderbilt D 1997 Spontaneous polarization and piezoelectric constants of III–V nitrides *Phys. Rev. B* **56** R10024–R7
[55] Tsubouchi K and Mikoshiba N 1985 Zero-temperature-coefficient SAW devices on AlN epitaxial films *IEEE Trans. Sonics Ultrason.* **32** 634–44
[56] Lundstrom M 2000 *Fundamentals of Carrier Transport* 2nd edn (Cambridge University Press)
[57] Vurgaftman I and Meyer J R 2003 Band parameters for nitrogen-containing semiconductors *J. Appl. Phys.* **94** 3675–96
[58] Vurgaftman I, Meyer J R and Ram-Mohan L R 2001 Band parameters for III–V compound semiconductors and their alloys *J. Appl. Phys.* **89** 5815–75
[59] Sarasamak K, Limpijumnong S and Lambrecht W R L 2010 Pressure-dependent elastic constants and sound velocities of wurtzite SiC, GaN, InN, ZnO, and CdSe, and their relation to the high-pressure phase transition: a first-principles study *Phys. Rev. B* **82** 035201
[60] Look D C and Sizelove J R 2001 Predicted maximum mobility in bulk GaN *Appl. Phys. Lett.* **79** 1133–5
[61] Bassaler J *et al* 2025 Al-rich AlGaN channel high electron mobility transistors on silicon: a relevant approach for high temperature stability of electron mobility *Adv. Electron. Mater.* **11** 2400069
[62] Zanato D, Gokden S, Balkan N, Ridley B K and Schaff W J 2004 The effect of interface-roughness and dislocation scattering on low temperature mobility of 2D electron gas in GaN/AlGaN *Semicond. Sci. Technol.* **19** 427
[63] Lee N-E, Zhou J-J, Chen H-Y and Bernardi M 2020 Ab initio electron-two-phonon scattering in GaAs from next-to-leading order perturbation theory *Nat. Commun.* **11** 1607
[64] Bhapkar U V and Shur M S 1997 Monte Carlo calculation of velocity-field characteristics of wurtzite GaN *J. Appl. Phys.* **82** 1649–55